ISBN: 978-3-95450-214-1 ISSN: 2673-5490 doi:10.18429/JACoW-IPAC2021-TUPAB417

PUSHING SPATIAL RESOLUTION LIMITS IN SINGLE-SHOT TIME-RESOLVED TRANSMISSION ELECTRON MICROSCOPY AT THE UCLA PEGASUS LABORATORY*

P. Denham†, P. Musumeci, Department of Physics and Astronomy,
University of California at Los Angeles, Los Angeles, CA, USA

Abstract

We present the design of a high-speed single shot relativistic electron microscope planned for implementation at the UCLA PEGASUS Laboratory capable of imaging with less than 30 nm spatial resolution and image acquisition time on the order of 10 ps. This work is based on a multi-cavity acceleration scheme for producing relativistic beams (3.75 MeV) with suppressed rms energy spread ($\sigma_\delta \approx 5e-5$), and a means to reduce smooth space charge aberrations by generating a quasi-optimal 4D particle distribution at the sample plane. start-to-end simulation results are used to validate the entire setup. Ultimately, a feasible working point is demonstrated.

INTRODUCTION

Transmission Electron Microscopy (TEM) has been an invaluable tool to probe the microscopic world [1–3]. With the aid of modern accelerator technology, TEM is on the verge of a paradigm shift as research groups implement in microscope columns RF driven high brightness electron sources [4]. These sources hold the potential to enable microscopy with nm resolution and ps acquisition times [5–8]. There is a big push for instruments having excellent spatio temporal resolution below 10 ps while maintaining sub-nm resolution as it will enable direct real-time visualization of processes in material sciences and biology currently beyond reach with current instruments [9–11].

The development of such instruments is hindered by some significant challenges. The main issue is the dominant interplay between beam current, spatial resolution, acquisition time, and contrast. Recent work provides details on optimizing the spatial resolution subject to the beam energy, contrast, and pulse duration [12]. In photoinjector-based microscopes, it is imperative to provide some means to manage the strong space charge effects associated with single-shot electron imaging. The analytical expressions for the space charge aberration coefficients reveal useful scaling laws that can be used to optimize the system. For a fixed contrast, higher energy, sample divergence, and lower current all improve the spatial resolution. This article expands on that work by applying it to a realistic setup envisioned for the UCLA PEGASUS photoinjector [13] whereby optimizing charge and illumination geometry at the sample, we seek to minimize spatial resolution for a pulse duration of ~10 ps.

* Work supported by DOE STTR grant No. DE-SC0013115 and by by the National Science Foundation under STROBE Science and Technology Center Grant No. DMR-1548924.
† pdenham@physics.ucla.edu

While stochastic scattering events also should be considered as they degrade resolution by introducing a random blur [14], for 10 ps beams with $\approx 10^7$ particle per pulse the collective field imparts strong correlations in the beam phase spaces which must be dealt with. In the case of elongated aspect ratio in the beam rest frame $\sigma_r/\gamma\sigma_z \ll 1$ (where σ_r is the transverse rms measure and σ_z is the longitudinal rms measure of the beam), the longitudinal dependence simplifies out, and the collective field essentially only depends on the 4D transverse distribution function. The 4D distribution function can be appropriately shaped with apertures and condensers to linearize the beam's mean space-charge fields through objective transport. The optimal case is a 4D uniformly filled ellipsoid, which is very challenging to deliver at the sample plane, thus here we consider the next best-case scenario which is a uniform momentum distribution at the sample to optimize an RF accelerator for high-speed microscopy.

We present start-to-end simulation results of an upcoming experiment planned for implementation at the 3.75 MeV PEGASUS beamline, demonstrating 30 nm spatial resolution is within reach with the existing hardware. We first estimate the optimum accelerator working point analytically, then follow up with particle tracking simulations starting from the cathode. The beamline includes a 1.6 Cell RF gun, followed by a linac booster for energy tuning and a 7 cell X-band cavity that compensates for RF-induced quadratic energy spread. The optimal distribution shape is generated using two condenser lenses and an optimally positioned aperture which combine to yield a Gaussian spatial distribution with a uniformly filled momentum space at the sample plane. This linearizes the collective field through objective transport.

ACCELERATOR WORKING POINT

In our study, the initial beam has a flat-top temporal profile with a full width of 10 ps. The transverse profile is a gaussian with σ = 50 μm. The RF gun is run with a peak field of 73 MV/m to provide a beam kinetic energy of 3.75 MeV, which is limited by the availability of focal lengths (5 cm) of the lenses and available distance in the radiation-shielded bunker. In the gun, different longitudinal slices of the beam experience different accelerating gradients, the effect of which, generates a longitudinal phase space correlation, $\delta\gamma/\gamma(\phi) \approx \phi^2/2$, where ϕ is the phase offset from the synchronous phase of the accelerator. This quadratic longitudinal phase space correlation leads to dramatic chromatic aberrations which must be suppressed.

ISBN: 978-3-95450-214-1 ISSN: 2673-5490 doi:10.18429/JACoW-IPAC2021-TUPAB417

A higher harmonic cavity is used to cancel the correlation as discussed in [5]. The net energy gain correlation through all 3 cavities can be expressed as:

$$\gamma(t) = \gamma_0 \cos(\omega_0 t) - \gamma_x cos(\omega_X t) + \gamma_L cos(\omega_0 t), \quad (1)$$

where t, is the time of arrival relative to the resonant particle, $\gamma_0, \gamma_L, \gamma_x$, are the energy gains and losses in the S-band gun, Linac, and x-band linearizer respectively. The cavity angular frequencies ω_0, ω_x are 2π(2.856 GHz), and 2π(9.6 GHz) respectively. The amplitude of the x-band is chosen to cancel the quadratic correlation in the Taylor expansion in Eq. (1), which can be expressed in terms of the energy gains and cavity frequencies as $\gamma_x/(\gamma_0 + \gamma_L) = 0.0885$. When the cavities satisfy this condition, the leading order longitudinal phase space correlation is $\delta\gamma/\gamma = -\omega_0^2\omega_X^2 t^4/24$ in the absence of space charge effects which would yield for an initial 10 ps flat-top distribution an RMS relative energy spread of $\sigma_\gamma \approx 1e-5$. In particle tracking simulations, that take into account space charge (both intra-beam scattering and mean-field) and transverse effects, the longitudinal emittance increases, and after compensation the energy spread at the sample is 5e-5.

With the nominal energy and energy spread determined, we can estimate the resolution of the instrument with the quadrature sum of the various aberrations contributions as prescribed in [12]:

$$\mathscr{R} = \sqrt{\left(C_c\sigma_\gamma\sigma_\theta\right)^2 + \left(C_s\sigma_\theta^3\right)^2 + \mathscr{R}_{sc}^2 + \frac{SNR^2}{Dose}}. \quad (2)$$

Each term in Eq. (2) (except the last) is the rms measure of the dynamical image plane deviations of the linear optics. C_c, and C_s are the lens' chromatic and spherical aberration coefficients respectively, σ_γ is the rms relative energy spread, σ_θ is the beam divergence. R_{sc} is the space charge aberration term, which can be expressed as:

$$\mathscr{R}_{sc}(I, \gamma, L, \sigma_\theta, \sigma_r, f) \sim \frac{KLg}{8\sigma_\theta}, \quad (3)$$

where $K = \frac{2I}{I_A\gamma^3\beta^3}$, is the beam perveance, I is the beam current, $I_A \approx 17kA$ is the Alfven current, L is the object to image plane distance, and g is a dimensionless parameter of order unity obtained from self-consistent integration of the equations of motion and is directly related to the space charge aberration coefficients. The g parameter depends on the beam distribution function and its evolution along the beamline. Shorter focal lengths reduce g. The final term proxies the desired pixel size of the detector, which must be less than or equal to the dynamical aberrations for the beam to be capable of generating an image in a single shot. We desired a signal to noise ratio $SNR = 5$, as set by the Rose criterion [15]. The signal term constrains the spot size from becoming too large as $Dose \propto N/\sigma_r^2$, where N is the number of electrons in the beam. Built into Eq. (2) is the assumption that all the image plane deviations are independent of each other. In reality, they are not, but the dependence is weak.

The order of magnitude of the spherical and chromatic aberration coefficients is the focal length. Thus, a beam with energy spread on the order of $5e-5$ and divergence of 3 mrad yields spherical to chromatic aberration ratio of $\sigma_\theta^2/\sigma_\delta = 1/10$. The chromatic to space charge aberration contributions are comparable. Thus, the main resolution figures to consider come from chromatic, and space charge.

We aim to generate a transverse phase space at the object plane which is uniform in momentum space and spatially Gaussian to improve the linearity of the space charge fields in the objective column. This can be achieved using an aperture in the condenser stage. In the following setup, the condenser system is comprised of a quadrupole triplet lens and followed by a solenoid lens. The condenser system is configured such that there is a $3\pi/2$ phase advance between the initial aperture and the object plane.

We optimize Eq. (2) concerning beam spot size and divergence to obtain the ideal sample illumination settings that are feasible. The space charge term is evaluated semi-analytically using matrix propagators. The results are shown in Fig. 1, and indicate that smaller emittance yields better resolution as long as $\sigma_r/f\sigma_\theta << 1$. For example, the optimization reveals that better than 40 nm resolution is achievable with transverse geometric emittance less than 4 nm·rad. The next section presents GPT simulations of the entire beamline where illumination in this range of the parameter space is achieved and the spatial resolution is calculated to be in close agreement with these estimates.

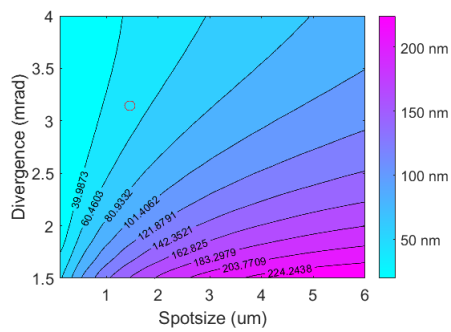

Figure 1: Optimization of condenser illumination geometry based on Eq. (2).

START-TO-END SIMULATIONS

The entire setup is simulated using the particle tracking code GPT [16]. For this simulation campaign, the nominal parameters are listed in Table 1. Initially, only the built-in spacecharge 3Dmesh model is used to capture the space charge forces and determine accelerator setpoints. After they are found, the simulations are redone using space charge 3D tree to include binary collisions. For now, we present results utilizing just the meshing algorithm. However, scattering effects from the source to the condenser, and in the projectors have been considered independently. The additional effects induce blurring but do not overwhelm the dynamics.

ISBN: 978-3-95450-214-1 ISSN: 2673-5490 doi:10.18429/JACoW-IPAC2021-TUPAB417

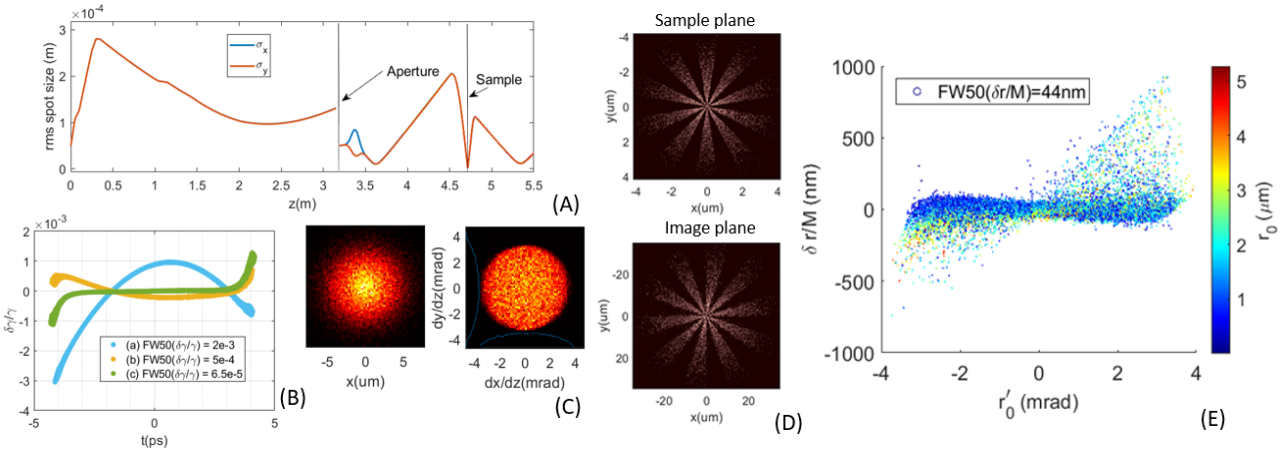

Figure 2: (A) Envelope evolution of the entire accelerator/microscope setup. (B) Longitudinal phase space evolution. (C) Sample plane distribution. (D) Object and image plane of Siemens star pattern. (E) Image deviation phase space.

Table 1: Beamline Parameters

Parameter	Value
MTE	0.5 eV
Charge	0.25 pC
Bunch Length (FWHM)	9.5 ps
Laser Spot Size	50 μm
X-band Peak Accelerating Gradient	6.7 MV/m
Linac Peak Accelerating Gradient	3 MV/m
1.6 Cell Gun Peak Accelerating Gradient	73 MV/m
Beam Kinetic Energy	3.75 MeV
Normalized Emittance	20 nm·rad

The envelope evolution throughout the entire simulation is shown in Fig. 2(A). The gun solenoid focuses the beam through the sequence of RF cavities meant to accelerate and minimize longitudinal emittance. In Fig. 2(B), the longitudinal phase space is shown at (a) the gun exit, (b) after X-band, and (c) at the sample plane. The chosen figure of merit to describe the overall energy spread of the beam is the FW50 measure, that is the full width of the distribution containing 50 percent of the particles. The final energy spread at the sample plane is $6.5e-5$, i.e, nearly 2 orders of magnitude smaller than at the gun exit. An aperture is placed at the entrance of the quadrupole triplet to select the uniform portion of the transverse phase space. Then the condenser system is set to swap the momentum and spatial distributions at the sample plane, yielding a uniform momentum distribution. The transverse phase space at the sample plane is shown in Fig. 2(C), where the final spot size is 1.5 μm with 3 mrad divergence.

The image plane deviations, $\delta r/M$, can be retrieved from GPT to obtain a general measure of the deviation space. In Fig. 2(C), the object and image planes are shown after imprinting a Siemens star pattern on the distribution at the sample plane. The pattern can be analyzed using a modulation transfer function as an alternative way to benchmark resolution. We directly measure the FW50 measure of the image plane deviations in Fig. 2(D) and obtain 44 nm.

The FW50 measure was minimized by choosing an optimal defocus. Also, the image plane deviations are correlated with initial axial distance, so this 4D distribution has better resolution at the core than at the edges of the field of view. This effect can also be seen in the Siemens star pattern, as the outskirts of the fans are significantly blurred compared to the sharper edges close to the core of the image. This effect is in part caused by the 3rd order space charge deflections being mainly imparted near the object plane. After the object plane, the beam spends a majority of the time as a uniform spatial distribution that has linear space charge forces, thus no 3rd order effects.

To improve resolution from here we can increase the pulse duration of the beam, or optimize the sample plane illumination. If the ideal illumination conditions could be achieved, initializing the same 4D distribution at the sample with smaller spot size, we would obtain a further resolution improvement. For example, if the spot size could be reduced below 1 μm, the resolution would be 30 nm. Even larger improvements could be achieved if we had available shorter focal length lenses ($f < 1.5$ cm) with smaller aberration coefficients [17], then simulations indicate that with the same injector, 10 nm or better could be achievable.

CONCLUSION

We have presented a high-speed microscope relying on a pulsed RF-gun-based high brightness electron source capable of delivering ~ 30 nm spatial resolution with a 10 ps exposure time. This work takes advantage of a recently developed analytical framework to describe collective space charge effects and guide the optimization of a realistic high-speed TEM setup. With a stronger objective lens, sub 10 nm resolution is achievable.

ISBN: 978-3-95450-214-1 ISSN: 2673-5490 doi:10.18429/JACoW-IPAC2021-TUPAB417

REFERENCES

[1] L. Reimer, *Transmission electron microscopy: physics of image formation and microanalysis*, Boston, MA, USA: Springer, 2013.

[2] J. C. Spence, *High-resolution electron microscopy*, Oxford, UK: Oxford Univ. Press, 2013.

[3] D. B. Williams and C. B. Carter, "The transmission electron microscope" in *Transmission electron microscopy*, Boston, MA, USA: Springer-Verlag, 1996, pp. 3–17.

[4] P. Musumeci *et al.*, "Advances in bright electron sources", *Nucl. Instrum. Methods. Phys. Res. A*, vol. 907, pp. 209–220, 2018. doi:10.1016/j.nima.2018.03.019

[5] R. Li and P. Musumeci, "Single-shot MeV transmission electron microscopy with picosecond temporal resolution", *Phys. Rev. Appl.*, vol. 2, no. 2, p. 024003, 2014. doi:10.1103/PhysRevApplied.2.024003

[6] D. Cesar *et al.*, "Demonstration of single-shot picosecond time-resolved MeV electron imaging using a compact permanent magnet quadrupole based lens", *Phys. Rev. Lett.*, vol. 117, no. 2, p. 024801, 2016. doi:10.1103/PhysRevLett.117.024801

[7] C. Lu *et al.*, "Imaging nanoscale spatial modulation of a relativistic electron beam with a MeV ultrafast electron microscope", *Appl. Phys. Lett.*, vol. 112, no. 11, p. 113102, 2018. doi:10.1063/1.5023179

[8] T. LaGrange *et al.*, "Single-shot dynamic transmission electron microscopy", *Appl. Phys. Lett.*, vol. 89, no. 4, p. 044105, 2006. doi:10.1063/1.2236263

[9] A. H. Zewail, "Four-dimensional electron microscopy", *Science*, vol. 328, no. 5975, pp. 187–193, 2010. doi:10.1126/science.1166135

[10] G. H. Campbell, J. T. McKeown, and M. K. Santal, "Time resolved electron microscopy for in situ experiments", *Appl. Phys. Rev.*, vol. 1, no. 4, p. 041101, 2014. doi:10.1063/1.4900509

[11] P. K. Olshin, G. Bongiovanni, M. Drabbels, and U. J. Loren, "Atomic-Resolution Imaging of Fast Nanoscale Dynamics with Bright Microsecond Electron Pulses", *Nano Lett.*, vol. 21, p. 612, 2020. doi:10.1021/acs.nanolett.0c04184

[12] P. Denham and P. Musumeci, "Space-Charge Aberrations in Single-Shot Time-Resolved Transmission Electron Microscopy", *Phys. Rev. Appl.*, vol. 15, p. 024050, 2021. doi:10.1103/PhysRevApplied.15.024050

[13] D. Alesini *et al.*, "New technology based on clamping for high gradient radio frequency photogun", *Phys. Rev. Applied*, vol. 18, no. 9, p. 092001, 2015. doi:10.1103/PhysRevSTAB.18.092001

[14] B. Reed *et al.*, "The evolution of ultrafast electron microscope instrumentation", *Microscopy and Microanalysis*, vol. 15, no. 4, p. 272, 2009. doi:10.1103/PhysRevSTAB.18.092001

[15] A. Rose, *Advances in Electronics and Electron Physics*, New York, NY, USA: Academic Press, 1948.

[16] G. Pöplau *et al.*, "Multigrid Algorithms for the Fast Calculation of Space-Charge Effects in Accelerator Design" *Magnetics, IEEE Transactions on*, vol. 40, no. 4, pp. 714-717, 2004. doi:10.1109/TMAG.2004.825415

[17] W. Wan, F. R. Chen, and Y. Zhu, "Design of compact ultrafast microscopes for single-and multi-shot imaging with MeV electrons", *Ultramicroscopy*, vol. 194, pp. 143–153, 2018. doi:10.1016/j.ultramic.2018.08.005